Physics of Fluids

RESEARCH ARTICLE | MARCH 08 2024

Fluid–acoustic interactions around an expanding pipe with orifice plates

Akitomo Fukuma (福間章友); Manato Kawai (川合央人); Nini Furukawa (古川新日); Kenji Kawasaki (川﨑賢二); Ichiro Yamagiwa (山極伊知郎) ; Masahito Nishikawara (西川原理仁) ; Hiroshi Yokoyama (横山博史)

Physics of Fluids 36, 036116 (2024)
https://doi.org/10.1063/5.0193029

Fluid–acoustic interactions around an expanding pipe with orifice plates

Cite as: Phys. Fluids **36**, 036116 (2024); doi: 10.1063/5.0193029
Submitted: 21 December 2023 · Accepted: 14 February 2024 ·
Published Online: 8 March 2024

Akitomo Fukuma (福間章友),[1] Manato Kawai (川合央人),[1] Nini Furukawa (古川新日),[1] Kenji Kawasaki (川崎賢二),[2] Ichiro Yamagiwa (山極伊知郎),[2] Masahito Nishikawara (西川原理仁),[1] and Hiroshi Yokoyama (横山博史)[1,a)]

AFFILIATIONS

[1]Department of Mechanical Engineering, Toyohashi University of Technology, Aichi 441-8580, Japan
[2]KOBE STEEL, LTD., 1-5-5 Takatsukadai, Nishi-ku, Kobe, Hyogo 651-2271, Japan

[a)]Author to whom correspondence should be addressed: h-yokoyama@me.tut.ac.jp

ABSTRACT

Expanding pipes with orifice plates are often utilized as silencers for fluid machinery. However, intense tonal sounds can be generated from a flow through such expanding pipes. To clarify the mechanism of tonal sound from a flow through a circular expanding pipe with two orifice plates and the conditions for intense acoustic radiation, the flow and acoustic fields are directly solved based on the compressible Navier–Stokes equations. Phase-averaged flow fields indicate the occurrence of periodic vortex shedding in the free shear layers of the expanding pipe, resulting in acoustic radiation. The effects of the orifice radius and freestream Mach number on the acoustic radiation are focused on. The computational results demonstrate that vortex rings or spiral vortices are generated in the cavities formed by the orifice plates, where the primary vortical shape changes, depending on the freestream Mach number and orifice radius. The collision of the vortex ring and spiral vortex with the orifice plate or downstream edge of the expanding pipe leads to the occurrence of circumferentially in-phase and one-wavelength-mode pressure fluctuations, respectively. The orifice radius also affects the convective velocity of vortices and the position of the acoustic source, varying the frequency of the acoustic radiation. The findings of this research provide the first clarifications of fluid–acoustic interactions in an expanding pipe with orifice plates.

I. INTRODUCTION

Expanding pipes or side branches[1] are often utilized as a silencer to reduce sound pressure fluctuations generated by fluid machinery. To enhance the sound reduction effects, orifice plates or perforated plates[2] are installed in many expanding pipes as silencers. However, tonal sounds can be generated from a flow through the expanding pipe with orifice plates. Thus, the mechanism and conditions for intense tonal acoustic radiation must be clarified. As shown in Fig. 1, an expanding pipe with orifice plates includes a series of axisymmetric cavities divided by the orifice plates.

Many researchers[3–9] have investigated the acoustic radiation from a flow over a two-dimensional rectangular cavity. Rossiter proposed the mechanism of self-sustained oscillations in such a cavity flow.[3] In this mechanism, the vortices shed from the upstream edge of the cavity impinge on the downstream edge, wherein acoustic waves are generated and propagated in the upstream direction. A new vortex is formed in the free shear layer owing to the acoustic feedback at the upstream edge. This mechanism was confirmed by direct aeroacoustic simulations based on the compressible Navier–Stokes equations.[4,5] Moreover, the self-sustained oscillations can be intensified by the coupling of the above-mentioned fluid–acoustic interactions in the shear layer with acoustic resonance in the cavity.[6–8] Rockwell and Naudascher[9] classified these self-sustained oscillations as fluid-resonant oscillations.

Studies[10–14] have also investigated self-sustained oscillations in an axisymmetric rectangular cavity without an orifice plate, where the cavity has a rectangular shape on the cross section with each circular angle. The series of experimental studies for a flow around an axisymmetric rectangular cavity by Aly and Ziada[10,11] demonstrated the excitation of a stationary or rotational diametral acoustic mode in the cavity depending on the freestream Mach number. Wang and Liu[12,13] showed by three-dimensional zonal compressible large eddy simulations that the rotational diametral acoustic mode was induced by spiral vortices shed in the shear layer in the axisymmetric cavity. Moreover, the compressible flow simulations by Abdelmwgoud *et al.*[14] showed that the stationary acoustic mode is induced by vortex rings or arch-shaped vortices.

Several studies[15–17] have also been conducted on the aerodynamic sound from a flow through an orifice plate. Matsuura and Nakano[15,16]

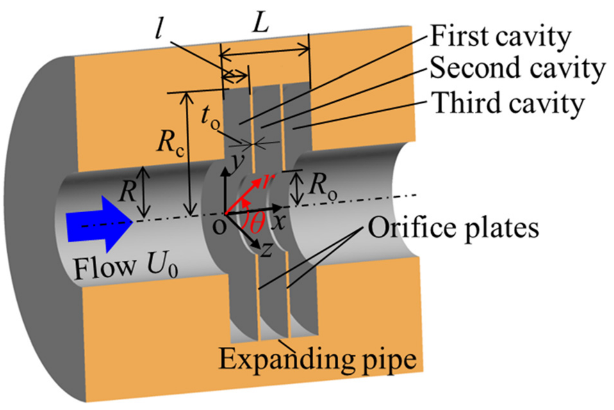

FIG. 1. Flow through an expanding pipe with orifice plates for the ratio of orifice radius, R_o, to the radius of upstream and downstream pipes connected with the expanding pipe, R, of $R_o/R = 0.7$, where half part of the model is shown for clarity.

investigated the radiation mechanism of tonal sound by the impingement of a flow issued from a circular nozzle with a downstream orifice plate with a hole (hole tone) through experiments and compressible flow simulations. The acoustic radiation was found to occur due to the collision of vortex rings with the edge of a downstream orifice plate. Sano and Oyaizu[17] visualized a flow around two closely installed orifice plates in a pipe along with sound measurement. They reported variations in tonal sound frequency with the inflow velocity, wherein the number of vortices between the two orifice plates was varied.

Although the above-mentioned studies investigated the flows around a cavity or orifice plate(s), the generation mechanism of tonal sounds from an expanding pipe installed with orifice plates has not been sufficiently investigated. The present research objective is to clarify the radiation mechanism and condition for the tonal sound for the flow through an expanding pipe with two orifice plates. For this purpose, fluid–acoustic interactions are directly simulated based on compressible Navier–Stokes equations along experimental studies. In particular, the effects of the orifice radius and freestream Mach number on the acoustic radiation are focused on. To the best of the authors' knowledge, this is the first time that the fluid–acoustic interactions around an expanding pipe with orifice plates have been clarified.

In Sec. II, the flow configurations and methodologies are described along with computational validation. The results and discussions are presented in Sec. III. The acoustic radiation from the flow around the expanding pipe is discussed for the orifice radius same as that of the pipe connected to the expanding pipe in Sec. III A. The effects of the freestream Mach number and orifice radius on the self-sustained oscillations are discussed in Secs. III B and III C, respectively. Finally, a brief summary is provided at the end of this paper.

II. METHODOLOGIES

A. Flow configurations

Figure 1 shows the configurations for a flow through an expanding pipe with two orifice plates. The coordinate system is defined with the origin at the center of the expanding pipe inlet. The x, r, and θ directions are in the streamwise, radial, and circumferential (counterclockwise from the upstream view) directions, respectively. The compressible flow simulations are based on a rectangular coordinate system with the x, y, and z axes, wherein the y and z axes are along $\theta = \pi/2$ and 0, respectively.

The radius of both the upstream and downstream pipes connected with the expanding pipe is $R = 25.2$ mm, and the radius of the expanding pipe is $R_c/R = 2.2$. The streamwise length of the expanding pipe is $L/R = 1.7$. In the computations, the orifice radius is set to $R_o/R = 0.7$, 1.0, and 1.3 for both orifice plates, and the plate thickness is constant at $t_o/L = 0.03$. These configurations were determined referring to the shape of the actual silencer.[18] To validate the computational accuracy, the predicted acoustic radiation is compared with the experimental results for the orifice radius of $R_o/R = 1.0$. The expanding pipe contains three cavities divided by the two orifice plates. These cavities are referred to as the first, second, and third cavities along the streamwise direction, where the cavity length is $l/L = 0.31$ for all the three cavities.

In the experiments, the freestream velocity was varied within the range of $U_0 = 10$–50 m/s considering the flow conditions for the installation of present expanding pipe as a silencer around the fluid machinery. This corresponds to the freestream Mach number of $M \equiv U_0/c = 0.03$–0.16 and the Reynolds numbers based on the expanding pipe length of $\mathrm{Re}_L \equiv U_0 L/\nu = 2.8 \times 10^4$–$1.4 \times 10^5$, where c is the speed of sound and ν is the kinematic viscosity. The computations were performed within $M = 0.07$–0.15, in which the frequency for the most intense tonal sound steeply changed in preliminary experiments. The instantaneous local Mach number was found to become higher than the triple of freestream Mach number in the small orifice ($R_o/R = 0.7$) as discussed in Sec. III C 2, and the present experiments and computations were performed in the flow conditions without generation of shock waves.

B. Experimental methods

Figure 2 shows the experimental setup, where two orifice plates of steel plate cold commercial were installed in the expanding pipe of polylactic acid resin. A diffuser section was connected with the downstream pipe of the expanding pipe for velocity decrease to suppress aerodynamic sound generation at the outlet of the pipe model. The overall pipe model was installed in an anechoic chamber with a volume of $730 \times 1300 \times 600\,\mathrm{mm}^3$, which was the same as the chamber used in the previous study.[19] A centrifugal fan (AH-1000, Showa Denki) connected to the downstream pipe of the diffuser was utilized to drive air flow.

Freestream velocity U_0 was measured using a pitot tube with differential manometer (DM-3501, Cosmo Instruments) in the upstream pipe ($x/L = -0.24$, $r = 0$), where the effects of the flow around the expanding flow on the velocity are small. The uncertainty of the flow velocity was 0.1 m/s, which corresponds to the variation of 0.2% at the freestream Mach number of 0.13. The sound pressure level was measured using a pressure sensor (8510B-2, Meggitt) at two positions on the bottom of the second cavity ($x/L = 0.5$, $r/R_c = 1.0$) and on the downstream pipe wall ($x/L = 1.7$, $r/R = 1.0$). The measurement time required for data acquisition was 30 s, and the sampling frequency was 80 kHz.

C. Computational methods

1. Governing equations and finite-difference scheme

In this study, simulations were performed based on the three-dimensional compressible Navier–Stokes equations to directly and

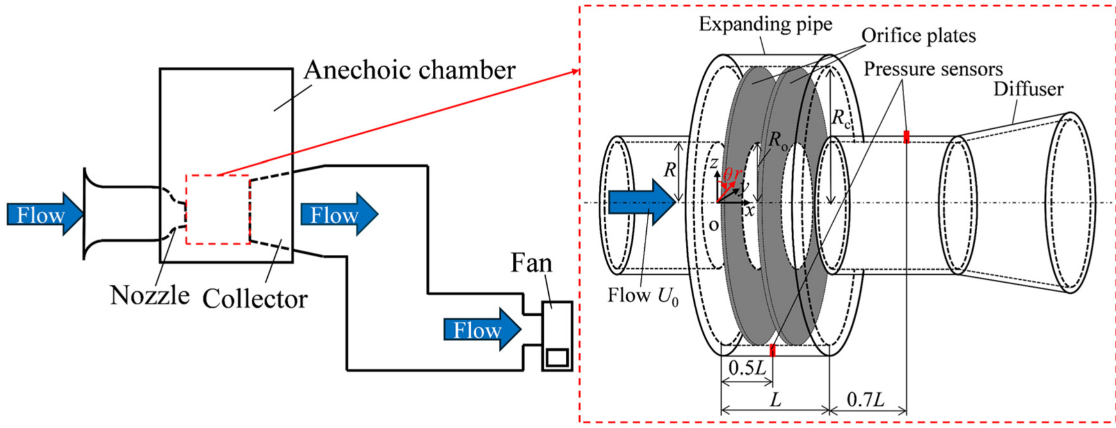

FIG. 2. Schematics of the experimental setup.

simultaneously predict the flow and acoustic fields for the flow around the expanding pipe with orifice plates. The interactions between flow and sound can be precisely predicted by direct aeroacoustic simulations compared with hybrid methods, which separately predict flow field (acoustic source) and acoustic propagation. In addition, the volume penalization method[20,21] was used to reproduce the overall pipe model, including the expanding pipe with orifice plates in a computational domain, as shown in Fig. 3. Penalization term $\boldsymbol{V}$ was added to the right-hand side of the governing equations as follows:

$$\boldsymbol{Q}_t + (\boldsymbol{E} - \boldsymbol{E}_{\rm v})_x + (\boldsymbol{F} - \boldsymbol{F}_{\rm v})_y + (\boldsymbol{G} - \boldsymbol{G}_{\rm v})_z = \boldsymbol{V}, \tag{1}$$

$$\boldsymbol{V} = -(1/\Phi - 1)\chi(\nabla \cdot \rho \boldsymbol{u}, 0, 0, 0, 0)^{\rm T}, \tag{2}$$

$$\Phi = 0.25, \tag{3}$$

where $\boldsymbol{Q} = (\rho, \rho u, \rho v, \rho w, \rho e)^{\rm T}$ is the vector of the conserved variables; $\boldsymbol{E}$, $\boldsymbol{F}$, and $\boldsymbol{G}$ represent the inviscid flux vectors; and $\boldsymbol{E}_{\rm v}$, $\boldsymbol{F}_{\rm v}$, and $\boldsymbol{G}_{\rm v}$ denote the viscous flux vectors. Variable χ was set to 0 outside the objects and 1 inside the objects. In the regions of $\chi = 1$, velocity was set to 0 and adiabatic change was assumed for relationship between the density and pressure. Coefficient Φ was set to 0.25 to ensure that the sound waves are almost completely reflected (reflectivity: 99%) on objects without computational unsteadiness.[21] These computational methods were confirmed to accurately predict the flow and acoustic fields around a circular pipe or a rotational fluid machinery.[21,22]

To accurately predict the generation and propagation of sound waves, a sixth-order-accurate compact scheme (fourth-order-accurate scheme at the boundaries)[23] was used for spatial discretization. Time integration was performed using a third-order-accurate Runge–Kutta method.

Large eddy simulations were performed to clarify the unsteady flow and acoustic fields without excessive computational cost. No explicit subgrid-scale (SGS) model was used, and a tenth-order spatial filter dissipated the turbulence energy in the grid scale, which should be transferred to the SGS eddies.[24] This filter also suppressed the numerical instabilities associated with the central differencing in the compact scheme. The coefficients of the filter were determined according to the values of those used by Gaitonde and Visbal.[25]

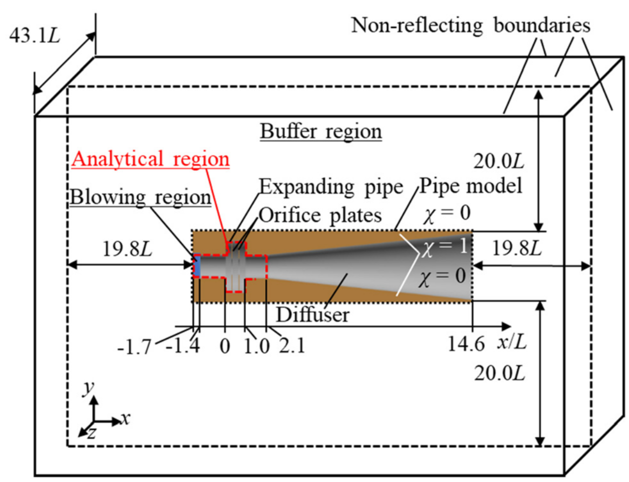

FIG. 3. Computational domain and boundary conditions, where a spanwise central cross-sectional view of the pipe model that includes the expanding pipe is shown.

2. Computational domain and boundary conditions

Figure 3 shows the computational domain and boundary conditions. The overall pipe model including the upstream, expanding, and downstream pipes with the diffuser like the experimental setup was set in the computational domain. The flow velocity was specified in a blowing region upstream of the expanding pipe ($x/L = -1.7$ to -1.4), as shown in Fig. 3, where this velocity specification method was utilized in the literature.[21] To prevent the reflection of sound waves on artificial boundaries, the nonreflecting boundary condition[26] was imposed on far outside boundaries from the pipe model.

As shown in Fig. 3, the analytical region was set around the expanding pipe, in which the predicted flow and sound were analyzed. In this region, the streamwise grid resolution in the expanding pipe was uniformly set to $\Delta x/l = 0.015$. The minimum grid spacings in the y and z directions around the cavities were $\Delta y_{\min}/l = \Delta z_{\min}/l = 0.023$. As discussed in Sec. II D, these grid resolutions were confirmed to be sufficiently fine to predict the tonal sounds by comparison of predicted results with those with a finer grid. The maximum streamwise grid spacing was $\Delta x/l = 0.15$ in the analytical region, with which more than 38 grid points were used per acoustic wavelength of the fundamental Strouhal number, $\mathrm{St} \equiv fl/U_0 = 1.35$ ($M = 0.13$ and $R_o/R = 0.7$), λ_f. By setting this resolution with the above-mentioned high-order discretization methods, acoustic propagation can be predicted for the frequency range to the fivefold of the fundamental frequency, where eight or more points per wavelength were confirmed to be enough to predict acoustic propagation.[5,23] A buffer region was set far from the expanding pipe, where the grid was stretched in all the directions to the maximum grid resolution of $\Delta/l = 6.3$ ($\Delta/\lambda_f = 1.1$ for $M = 0.13$ and $R_o/R = 0.7$) to dissipate acoustic and vortical disturbances near the artificial boundaries. The reflection of the sound at the outlet of the overall pipe model was confirmed to be negligibly small in the predicted results owing to the installation of the diffuser and above-mentioned grid stretching in the downstream region of the expanding pipe. This is consistent with the experimental acoustic conditions, where the duct with acoustic materials was connected to the downstream diffuser of the expanding pipe to prevent the acoustic reflection.

3. Initial flow field

A uniform flow field with zero velocity was set overall in the computational domain as the initial flow field. The pressure and density were set to those of standard air at 293 K. The predicted flow field and sound pressure presented in this paper were analyzed using the data obtained after the computational flow development of $40L/U_0$ from the initial field. The duration time for the spectral analysis was approximately $100L/U_0$ in the computation.

D. Computational validation

The present computational result ($\Delta y_{\min}/l = \Delta z_{\min}/l = 0.023$, total grid points of 66×10^6) is compared with that of the finer grid of $\Delta y_{\min}/l = \Delta z_{\min}/l = 0.015$ (total grid points of 110×10^6) to investigate the effects of grid resolution on the prediction accuracy, where the grid points for the region in the expanding pipe are changed approximately twice. Figure 4 shows the predicted sound pressure spectra with the present and finer grids at the flow condition for the intense acoustic radiation of $M = 0.12$ and $R_o/R = 1.0$. The Strouhal resolution of the spectral analysis is $\Delta\mathrm{St} = 0.013$, where the data are averaged about ten times in time. At higher Strouhal numbers than $\mathrm{St} = 2.0$, the Strouhal numbers for tonal sounds with finer grids are slightly lower than those with present grids. This is possibly because finer vortices are captured by the computation with finer grids, which is indicated by the increase in the floor level of the sound pressure spectrum in high Strouhal number range of $\mathrm{St} > 2$, and the convection path and velocity for large-scale vortices related to the tonal sounds are affected. However, the most intense acoustic radiation occurs at the fundamental Strouhal number of $\mathrm{St} = 0.5$, as shown in both spectra. The spectrum predicted with the present grid agrees well with that of the finer grid.

Moreover, the predicted sound pressure is compared with that measured for $M = 0.13$ and $R_o/R = 1.0$. Figure 5 shows the predicted and measured sound pressure spectra at the bottom of the second cavity ($x/L = 0.5$, $r/R_c = 1.0$) at $M = 0.13$, where the data were averaged 10 and 1300 times in time for the computation and experiment,

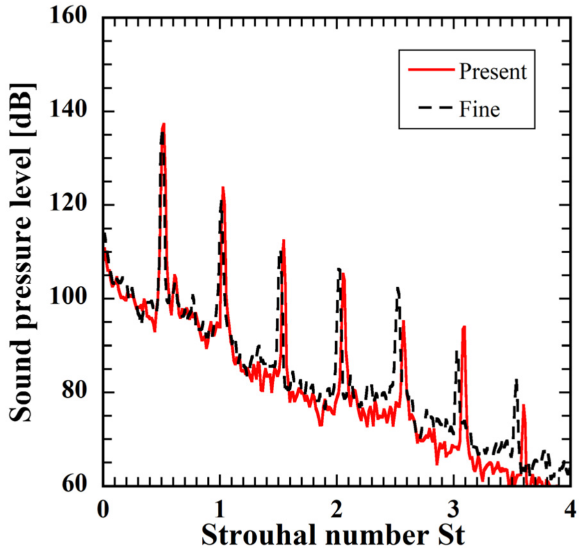

FIG. 4. Predicted sound pressure spectra at the bottom of the second cavity ($x/L = 0.5$, $r/R_c = 1.0$) at $M = 0.12$ for $R_o/R = 1.0$, where the present computational result with $\Delta y_{\min}/l = \Delta z_{\min}/l = 0.023$ is compared with that using a finer grid of $\Delta y_{\min}/l = \Delta z_{\min}/l = 0.015$.

respectively. To consider the difference in the averaging number (low-frequency time variation), the variances of the measured sound pressure levels with the same averaging number as that of the computation are represented with bars in Fig. 5. It is presented that the intense peaks of tonal sounds appear at the fundamental Strouhal number of $\mathrm{St} = 0.5$ and higher harmonic Strouhal numbers in both the predicted and measured spectra. The predicted sound pressure spectrum

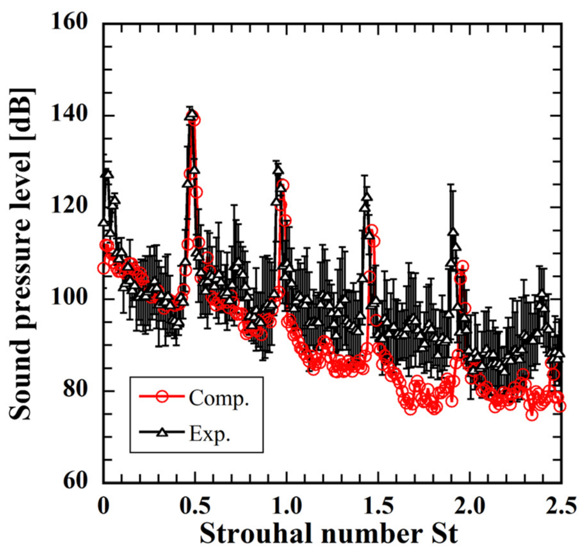

FIG. 5. Predicted and measured sound pressure spectra at the bottom of the second cavity ($x/L = 0.5$, $r/R_c = 1$) at $M = 0.13$ for $R_o/R = 1.0$, where variations of measured level with the same averaging number as that of the computation were represented with bars.

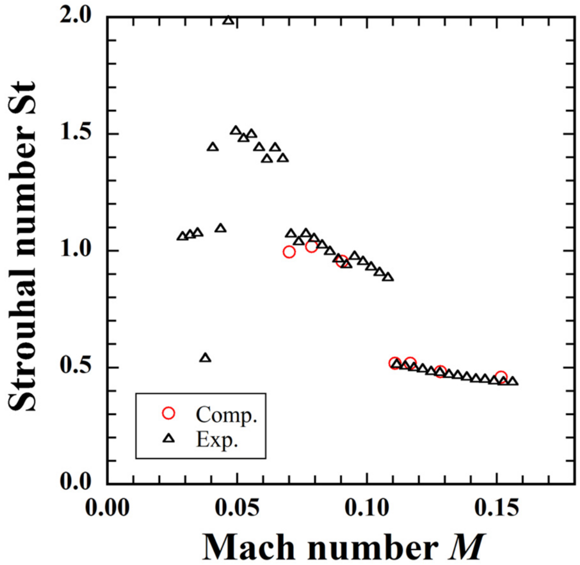

FIG. 6. Variations of the predicted and measured Strouhal numbers for the most intense tonal sound in the second cavity ($x/L = 0.5$, $r/R_c = 1.0$) with the freestream Mach number.

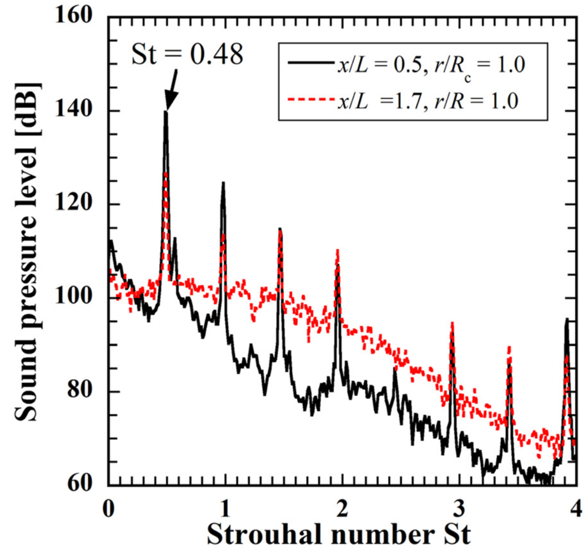

FIG. 7. Predicted sound pressure spectra on the bottom of the second cavity ($x/L = 0.5$, $r/R_c = 1.0$) and on the downstream pipe wall ($x/L = 1.7$, $r/R = 1.0$) for $R_o/R = 1.0$ and $M = 0.13$.

approximately agrees well with that measured considering the variations of the measured values.

Figure 6 shows the variations of the predicted and measured Strouhal number for the most intense tonal sound at the bottom of the second cavity ($x/L = 0.5$, $r/R_c = 1.0$) with the freestream Mach number. In both the predicted and measured variations, the Strouhal number is approximately 0.5 for relatively high Mach numbers of $M \geq 0.11$. The Strouhal number steeply changes (jumps) to $\mathrm{St} \approx 1.0$ for the lower Mach numbers, which is well reproduced with the present computation. It is noted that the acoustic radiation becomes relatively weaker and the Strouhal number for the largest sound becomes unstable at a low Mach number of $M < 0.06$ in the experiments. Based on the discussions in this section, it is concluded that the present computations adequately capture the acoustic radiation from a flow through an expanding pipe with orifice plates.

III. RESULTS AND DISCUSSION

A. Acoustic radiation due to vortices ($R_o/R = 1.0$)

In this section, the acoustic radiation and related flow behaviors with the condition of intense acoustic radiation of $R/R_o = 1.0$ and $M = 0.13$. Figure 7 shows the sound pressure spectra at the two positions on the expanding pipe ($x/L = 0.5$, $r/R_c = 1.0$) and on the downstream pipe wall ($x/L = 1.7$, $r/R = 1.0$). As shown in Fig. 7, the most intense tonal sound is generated at $\mathrm{St} = 0.48$ inside the expanding pipe and propagated into the downstream pipe. In this paper, the Strouhal number (frequency) for the most intense tonal sound on the

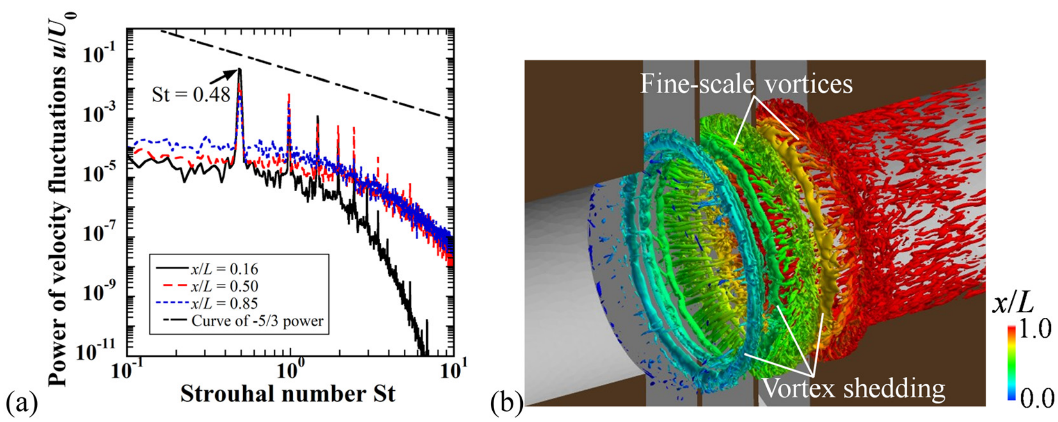

FIG. 8. Velocity fluctuations with vortex shedding in shear layer in the cavities at $M = 0.13$ for $R_o/R = 1.0$. (a) Predicted power spectra of velocity fluctuations, u/U_0, at the radial position for the most intense power at the fundamental Strouhal number of $\mathrm{St} = 0.48$ ($r/R = 0.96$, 0.99, 0.94 for $x/L = 0.16$, 0.50, 0.85). (b) Vortices represented by instantaneous iso-surfaces of second invariant of the velocity gradient tensor of $q/(U_0/l)^2 = 6.1$, which are colored by the value of x/L for clarity.

downstream pipe wall ($x/L = 1.7$, $r/R = 1.0$) is termed as the fundamental Strouhal number (frequency). As shown in Fig. 7, the sound pressure level in the broadband frequency range higher than the fundamental frequency becomes larger in the downstream pipe compared with that in the expanding pipe. This is because the flow turbulence generated in the expanding pipe is convected into the downstream pipe and induces turbulent pressure fluctuations on the wall of the downstream pipe.

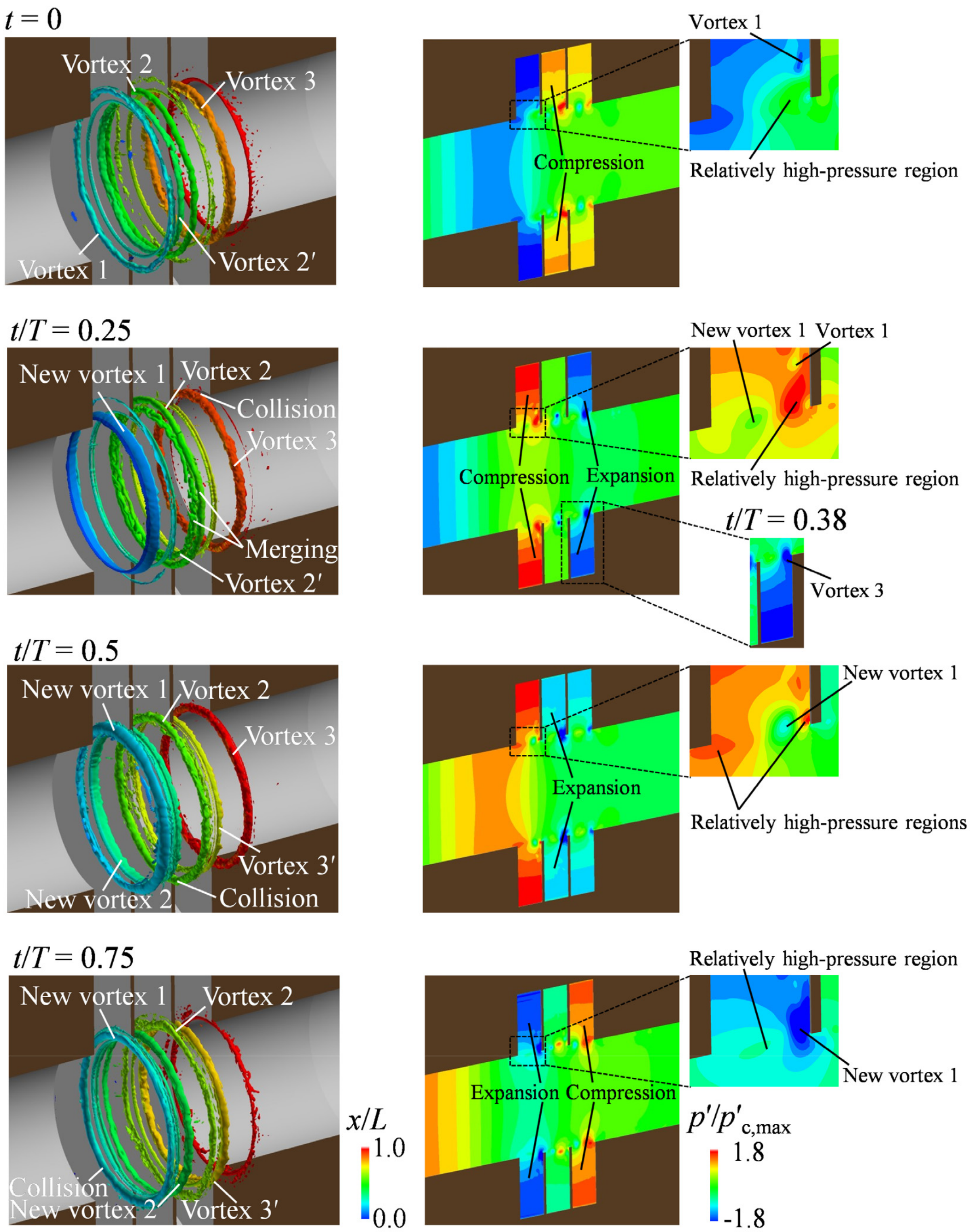

FIG. 9. Predicted phase-averaged flow and acoustic fields for the fundamental Strouhal number of St = 0.48 at $M = 0.13$ for $R_o/R = 1.0$, where T is time period and $t = 0$ is the phase for maximum pressure at the bottom of the second cavity ($x/L = 0.5$, $r/R_c = 1.0$), $p'_{c,max} = 380$ Pa. The left and right figures show vortices represented by the iso-surfaces of the second invariant of the velocity gradient tensor of $q/(U_0/l)^2 = 6.1$, which are colored by x/L, and the contours of fluctuation pressure on the x–r plane, respectively.

Figure 8(a) shows the power spectra of velocity fluctuations at the radial position for the maximum power at the fundamental frequency of $r/R = 0.96$, 0.99, and 0.94 for $x/L = 0.16$ (first cavity), 0.50 (second cavity), and 0.85 (third cavity), respectively. These positions are corresponding to the path of convection of the vortices related to the tonal sounds. As shown in Fig. 8, intense velocity fluctuations occur at $\mathrm{St} = 0.48$ for all cavities. Figure 8(b) shows the vortex structures represented by the instantaneous iso-surfaces of the second invariant of velocity gradient tensor, q. The periodic vortex shedding appears in the shear layers in the cavities, which corresponds to the intense power of velocity fluctuations at the fundamental Strouhal number of $\mathrm{St} = 0.48$ in Fig. 8(a). It is shown in Fig. 8(a), that the power in the broadband frequency range becomes higher along the curve of $-5/3$ power for the second and third cavities than that for the first cavity. This result is also consistent with the occurrence of fine-scale turbulent vortices in the flow around the second and third cavities, as shown in Fig. 8(b).

Figure 9 shows the phase-averaged flow fields, which were calculated by averaging the predicted fields 20 times for each phase in the time period T for the fundamental Strouhal number of $\mathrm{St} = 0.48$. The vortices and contours of fluctuation pressure at different phases are shown in the left and right figures, where $t = 0$ corresponds to the phase for the occurrence of the maximum pressure at the bottom of the second cavity, $p'_{c,\max}$.

As shown in Fig. 9, vortex rings with low-pressure regions and relatively high-pressure regions between the vortices are formed in the shear layers in the cavities (vortices 1, 2, and 3 for the first, second, and third cavities, respectively, at $t = 0$ in the left figure). The shedding of the vortex rings causes intense velocity fluctuations at the fundamental Strouhal number, as shown in Fig. 8(a). Furthermore, another vortex (Vortex 2′) appears in the second cavity at $t = 0$, Vortex 1 and Vortex 2′ originate from the same vortex in the first cavity and are generated by the splitting of the vortex due to the collision with the first orifice plate at $t/T = -0.25$ (0.75). At $t/T = 0.25$, a new vortex (new Vortex 1) is shed in the first cavity from the upstream edge of the expanding pipe, where relatively high-pressure regions become more compressed due to the small distance between Vortex 1 and new Vortex 1 near the first orifice plate as shown in Fig. 9. The interactions of the vortex and orifice edge lead to the intense pressure fluctuations around the orifice edge. Moreover, intense pressure fluctuations occur inside the cavity, where the cavity bottom (inner wall of expanding pipe) corresponds to the anti-node of pressure fluctuations by the standing wave.

Figure 10 shows the radial phase distributions of pressure fluctuations at the fundamental Strouhal number ($\mathrm{St} = 0.48$) along the streamwise position of the upstream surface of the first orifice plate ($x/l = 1.0$). As shown in Fig. 10, the pressure fluctuations are propagated from the region near the orifice edge to the inside and outside regions of the cavity. The almost in-phase pressure fluctuations occur in the region of $r/R_c \geq 0.6$ inside the cavity, indicating the formation of the standing wave in the depth direction of the cavity. These results indicate that the pressure fluctuations generated around the orifice edge cause the standing waves to form, leading to the compression and expansion in the entire region of the cavity.

As shown in Fig. 9 ($t/T = 0.25$), the vortex with the low-pressure region (Vortex 3) starts to be collided with the downstream wall of the expanding pipe and deformed with the spread of the low-pressure regions, which radiates an expansion wave.[5] The expansion wave is propagated inside the cavity, leading to the formation of standing waves and the occurrence of the expansion in the entire region of the third cavity. After the collision of the vortex, the pressure becomes lowest at the bottom of the third cavity at $t/T = 0.38$. Compared with the above-mentioned pressure fluctuations in the first cavity, intense pressure fluctuations occur with the almost opposite-phase relationship between the first and third cavities. At $t/T = 0.5$, the expansion occurs owing to the collision of Vortex 2 with the second orifice plate in the second cavity, and the compression wave that is radiated in the first cavity at $t/T = 0.25$ is propagated into the upstream pipe. In the second cavity, the pressure fluctuations from the three cavities are interfered with the above-mentioned phase difference, leading to slightly weaker pressure fluctuations than those in the other cavities.

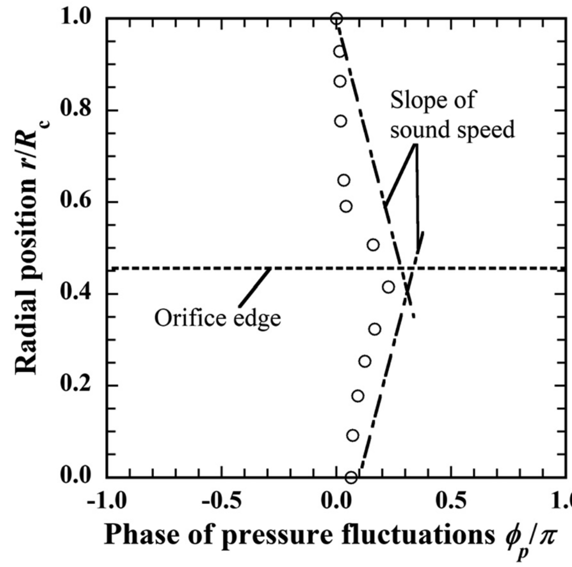

FIG. 10. Predicted radial phase distributions of pressure fluctuations at the fundamental Strouhal number ($\mathrm{St} = 0.48$) along the streamwise position of the upstream surface of the first orifice plate ($x/l = 1.0$) at $M = 0.13$ for $R_o/R = 1.0$ with reference to the phase at the bottom of the first cavity ($r/R_c = 1.0$).

Figure 11 shows the streamwise distribution of the phase in the streamwise velocity fluctuations, u, at the fundamental Strouhal number ($\mathrm{St} = 0.48$) in the shear layer in the second cavity. The slope of the phase indicates the convection of the vortices, as shown in Fig. 9, and the ratio of the convection velocity of vortices to the freestream velocity is estimated to be $\kappa \equiv U_c/U_0 = 0.6$. This value of κ is within the range of the values in the literature.[27,28]

B. Effects of Mach number on self-sustained oscillations ($R_o/R = 1.0$)

In this section, the variation of the self-sustained oscillations in the expanding pipe with the freestream Mach number is discussed for $R_o/R = 1.0$. Figures 12(a) and 12(b) show the sound pressure spectra at the two positions on the bottom of the second cavity ($x/L = 0.5$) and on the downstream pipe wall ($x/L = 1.7$), respectively. As shown in Fig. 12(a), the Strouhal number of the most intense sound at the bottom of the second cavity is $\mathrm{St} = 1.0$ at $M = 0.08$ and 0.09, whereas $\mathrm{St} = 0.5$ for the relatively high Mach numbers of $M = 0.11$ and 0.13.

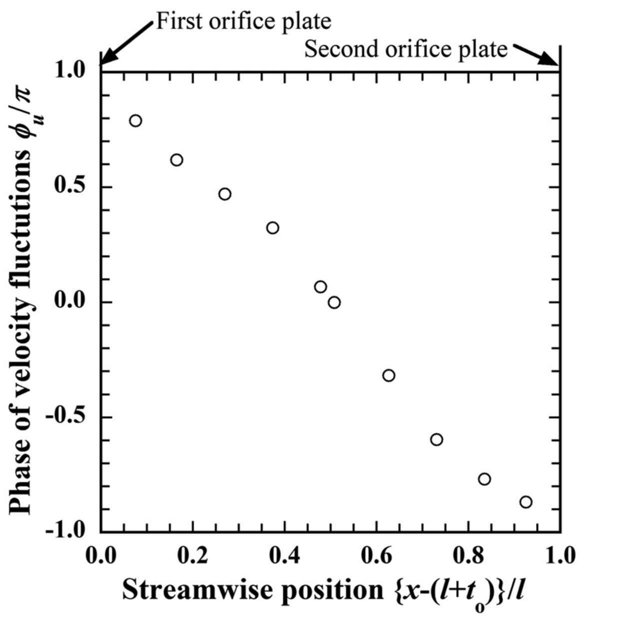

FIG. 11. Predicted streamwise distribution of the phase in streamwise velocity, u, at the fundamental Strouhal number (St = 0.48) in the shear layer in the second cavity at $M = 0.13$ for $R_o/R = 1.0$ with reference to the phase at the streamwise center of the second cavity of $\{x-(l+t_o)\}/l = 0.5$.

Meanwhile, as shown in Fig. 12(b), the tonal sound at St = 0.5 is most intensely propagated into the downstream pipe for all Mach numbers.

Figure 13(a) shows the circumferential phase distribution of pressure fluctuations at the Strouhal number for the intense tonal sound on the bottom of the second cavity at different Mach numbers. The phase of pressure fluctuations varies by 2π in a full circle for the Mach numbers of $M = 0.07$, 0.08 and 0.15, while the phase is circumferentially uniform at $M = 0.12$ and 0.13. The phase distributions for $M = 0.07$, 0.08 and 0.15 indicate the occurrence of the rotational acoustic mode[10,11] of $(m_r, m_c) = (0, 1)$ [acoustic mode (0, 1)].

Figure 13(b) shows the circumferential phase distribution of pressure fluctuations at $M = 0.08$ for the Strouhal numbers of St = 0.52 and 1.02, which are those for the most intense sound on the downstream pipe wall ($x/L = 1.7$, $r/R = 1.0$) and on the bottom of the second cavity ($x/L = 0.5$, $r/R_c = 1.0$), respectively. The pressure fluctuations with the approximately uniform phase in the circumferential direction occur at St = 0.52 in contrast to St = 1.02. This indicates the existence of the pressure fluctuations with different phase distributions. Meanwhile, the circumferential phase-varied sound is not likely to be propagated downstream compared with that with the uniform phase. Therefore, the tonal sound at St = 0.52 is more intensely propagated into the downstream pipe compared with St = 1.02, as shown in Fig. 12(b).

Figure 14 shows the variation of the Strouhal number for the most intense sounds inside and outside the expanding pipe with the freestream Mach number. In this figure, the curves of the Strouhal number for the shear layer oscillations proposed by Rossiter[3] (shear layer mode) are also presented, where the Strouhal number was estimated by the following equation:

$$\mathrm{St} = \frac{n-\gamma}{1/\kappa + M}, \tag{4}$$

where n is a positive integer (Rossiter mode number), and κ is set to 0.6 referring to the actual vortex convection velocity, as discussed in Sec. III A. Furthermore, the phase correction constant of $\gamma = 0.18$ is used for the curve to be fitted to the computational and measured Strouhal numbers. This value is within the value range of $\gamma = 0$–0.3, in the literature.[27] As shown in Fig. 14, the jump of the Strouhal number from St = 1.0 to 0.5 for the increase in the Mach number from $M = 0.09$ to 0.11 in the expanding pipe ($x/L = 0.5$, $r/R_c = 1$) corresponds to the change of the Rossiter mode from $n = 2$ to 1. As shown in Fig. 11 ($M = 0.13$), the phase of velocity fluctuations is approximately varied by 2π for cavity length l, which also confirms the occurrence of the Rossiter mode of $n = 1$ at the relatively high Mach number of $M = 0.13$.

Figure 14 also shows the curve of the Strouhal number for the acoustic mode occurring in the expanding pipe in the present simulations. The frequency for the acoustic mode is estimated for the present expanding pipe with orifice plates by that for a simple circular pipe[29] modified by the correction coefficient ε as follows:

$$f_{(m_r,m_c)} = \frac{c}{2}\frac{\alpha_{(m_r,m_c)}}{R_c}\varepsilon, \tag{5}$$

where m_r and m_c are the radial and circumferential mode numbers, respectively, and $\alpha_{(m_r,m_c)}$ is the Bessel coefficient. In addition, the correction constant of $\varepsilon = 1.1$ is estimated for the curve to be fitted to the predicted Strouhal numbers at which the first circumferential acoustic mode (0, 1) was confirmed to occur based on the phase distributions of the pressure fluctuations in the expanding pipe as shown in Fig. 13(a) (St = 1.04, 1.02, 0.96, 0.49 for $M = 0.07$, 0.08, 0.09, 0.15), by considering the effects of the complex shape of the present expanding pipe with the orifice plates on the acoustic mode. It is noted that these Strouhal numbers do not necessarily agree with those for the most intense tonal sounds at all the Mach numbers. Figure 14 shows that the above-mentioned jump of the Strouhal number for the most intense tonal sound in the expanding pipe between $M = 0.09$ and 0.11 occurs along the curve for the acoustic mode (0, 1) of $f_{(0,1)} = 2.0$ kHz.

Figure 15 shows the phase-averaged flow and acoustic fields for St = 1.02. As shown in Fig. 15(a), the spiral vortex is found to be formed in the shear layers in the expanding pipe. The collisions of the spiral vortices with the first and second orifice plates at $\theta = 3\pi/2$ and $\pi/2$, respectively, lead to the radiation of expansion waves from the orifice edges and the occurrence of the expansion in the cross sections of $\theta = 3\pi/2$ and $\pi/2$ in each cavity, as shown in Fig. 15(b). Moreover, compression occurs because of the interactions of the high-pressure regions between the vortices with the orifice plates at $\theta = \pi/2$ and $3\pi/2$ in the first and second cavities, respectively. When the spiral vortices are collided with the orifice edges, the expansion and compression waves are radiated with the above-mentioned circumferential phase difference because of the circumferential time variation for the collision of the vortices and high-pressure regions. The propagation of these waves into the cavities leads to the acoustic mode occurring in the entire cavities. The circumferentially anti-phase behavior is consistent with the acoustic phase distributions as shown in Fig. 13. Figure 15(b) shows the formation of two vortices with low-pressure regions in each shear layer of the first and second cavities, which indicates the occurrence of the second shear layer mode ($n = 2$). Figure 15(c) shows the contours of the fluctuation pressure and velocity vectors on the

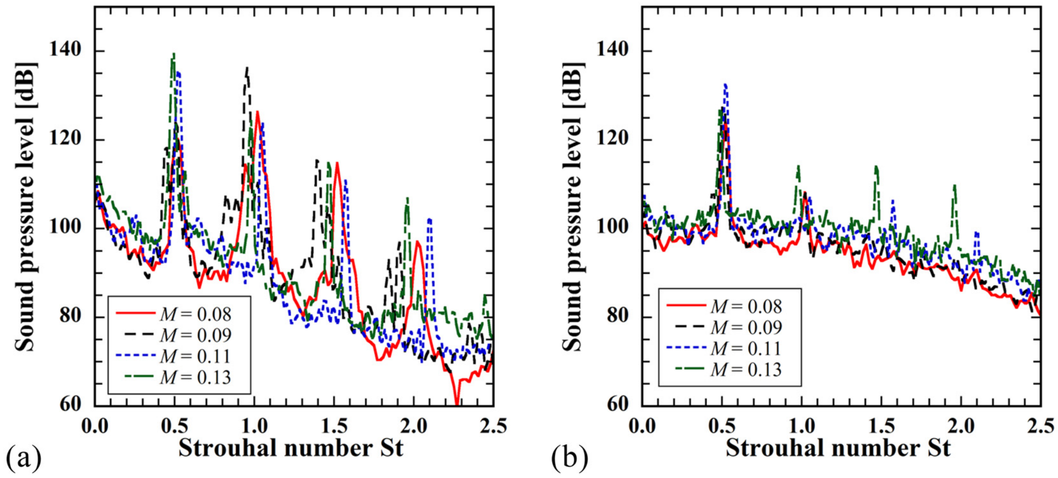

FIG. 12. Predicted acoustic radiation for different freestream Mach numbers for $R_o/R = 1.0$. (a) Sound pressure spectra on the second cavity bottom ($x/L = 0.5$, $r/R_c = 1.0$). (b) Sound pressure spectra on downstream pipe wall ($x/L = 1.7$, $r/R = 1.0$).

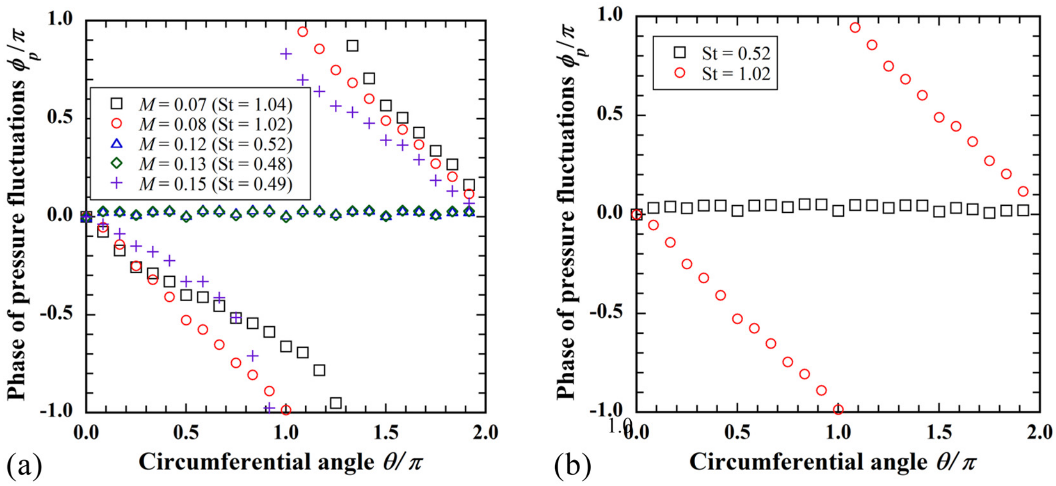

FIG. 13. Predicted circumferential phase distributions of pressure fluctuations on the second cavity bottom ($x/L = 0.5$, $r/R_c = 1.0$) with reference to the phase at $\theta = 0$. (a) Phase distributions for the intense sound at the second cavity bottom at different Mach numbers. (b) Phase distributions for the most intense sounds on the downstream pipe wall (St = 0.52) and the second cavity bottom (St = 1.02) at $M = 0.08$.

cross section of expanding pipe inlet ($x = 0$). The one-directional acoustic particle velocity in the cross section is generated due to the sound pressure fluctuations with the acoustic mode (0, 1), where the direction of the velocity fluctuations rotates due to the rotational acoustic mode. The shedding of vortices is excited by these acoustic velocity fluctuations as the acoustic feedback,[3,5] and the anti-phase acoustic feedback occurs between points with the circumferential angle difference of $\Delta\theta = \pi$. As a result, the second shear layer mode with spiral vortices occur by the rotational acoustic mode, where the Rossiter mode number is basically determined by the Strouhal number corresponding to the acoustic mode. These results confirm the occurrence of the fluid-resonant oscillations[9] due to the coupling of the second shear layer mode and acoustic mode (0, 1).

C. Self-sustained oscillations with different orifice radii

1. Variation of acoustic radiation

Figure 16 shows the sound pressure spectra with orifice radii of $R_o/R = 0.7$, 1.0, and 1.3 at $M = 0.13$. The most intense tonal sound occurs at St = 1.35 and 0.48 in the expanding pipe ($x/L = 0.5$, $r/R_c = 1.0$) for $R_o/R = 0.7$ and 1.0, respectively, as shown in Fig. 16(a). Moreover, these sounds are intensely propagated into the downstream pipe, as shown in Fig. 16(b). On the other hand, in the case of $R_o/R = 1.3$, the most intense tonal sound occurring at St = 0.57 in the expanding pipe becomes weak in the downstream pipe, where the fundamental Strouhal number for the most intense tonal sound is St = 0.28.

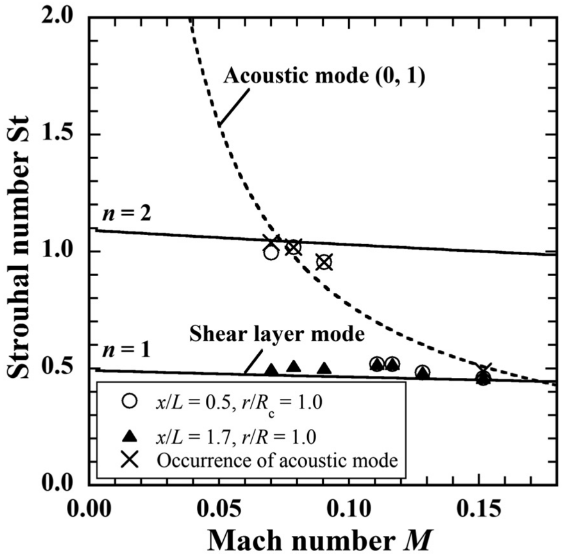

FIG. 14. Variation of Strouhal number with the freestream Mach number for the most intense tonal sounds on the second cavity bottom ($x/L = 0.5$, $r/R_c = 1.0$) and on downstream pipe wall ($x/L = 1.7$, $r/R = 1.0$) and those for the occurrence of acoustic mode (0, 1) based on the pressure phase distributions ($x/L = 0.5$, $r/R_c = 1.0$), where the curves for shear layer and acoustic modes by Eqs. (4) and (5) are also shown.

Figure 17 shows the circumferential phase distribution of the pressure fluctuations on the bottom of the second cavity. As shown in Fig. 17, the phase of pressure fluctuations at St = 0.57 for $R_o/R = 1.3$ is steeply varied around $\theta/\pi = 0.65$ and 1.65 by π, which indicates the occurrence of the stationary acoustic mode (0, 1)[10,11] with the generation of circumferential standing waves. Figure 17 also shows the sketches of the relationship between vortical structures and acoustic modes. These pressure fluctuations for the stationary acoustic mode (0, 1) occur due to the shedding of arch-shaped vortices discussed in the next paragraph, while the spiral vortices lead to the pressure fluctuations with the rotational acoustic mode (0, 1) as shown in Figs. 13 and 15. Meanwhile, the pressure fluctuations at St = 1.35 ($R_o/R = 0.7$), 0.48 ($R_o/R = 1.0$), and 0.28 ($R_o/R = 1.3$) show an almost in-phase behavior in the circumferential direction. Taking the variation of the sound pressure spectra with the position inside and outside the expanding pipe shown in Fig. 16 into consideration, it is indicated that the sound with in-phase behaviors is intensely propagated into the downstream pipe compared with circumferentially varied-phase distributions. This is consistent with the relationship between the phase distributions of the pressure fluctuations and propagation into the downstream pipe at St = 0.52 and 1.02 for $R_o/R = 1.0$ and $M = 0.08$, as discussed in Sec. III B.

Figure 18 shows the phase-averaged flow and fluctuation pressure field at the fundamental Strouhal numbers of St = 1.35 and 0.28 for $R_o/R = 0.7$ and 1.3, respectively, where the vortices with low-pressure regions are shown by the iso-surfaces of fluctuation pressure. As

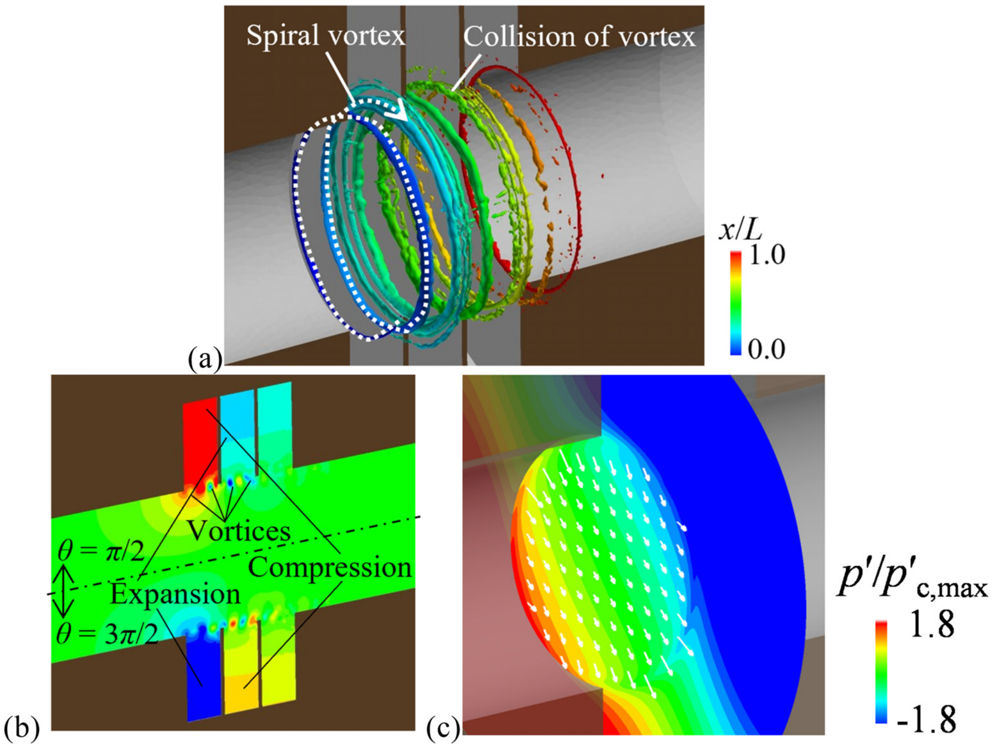

FIG. 15. Predicted phase-averaged flow and acoustic fields for St = 1.02 at $M = 0.08$ ($R_o/R = 1.0$). (a) Vortices represented by the iso-surfaces of the second invariant, $q/(U_0/l)^2 = 6.1$ colored by x/L at the time for the collision of the vortex with the second orifice plate at $\theta = \pi/2$ ($t/T = 0.5$). (b) Contours of the fluctuation pressure $p'/p'_{c,max}$ ($p'_{c,max}$ = 75 Pa) on the x–r plane at $t/T = 0.5$. (c) Contours of the fluctuation pressure and fluctuation velocity vectors on the cross section of expanding pipe inlet ($x = 0$) at $t/T = 0.75$.

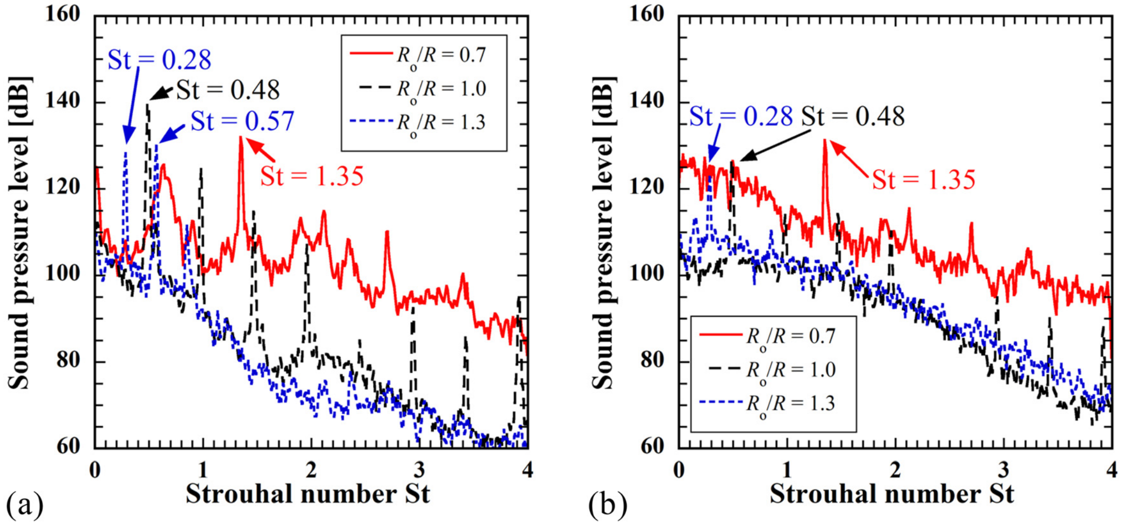

FIG. 16. Predicted sound pressure spectra at $M = 0.13$ with different orifice radii, R_o. (a) Second cavity bottom ($x/L = 0.5$, $r/R_c = 1.0$). (b) Downstream pipe wall ($x/L = 1.7$, $r/R = 1.0$).

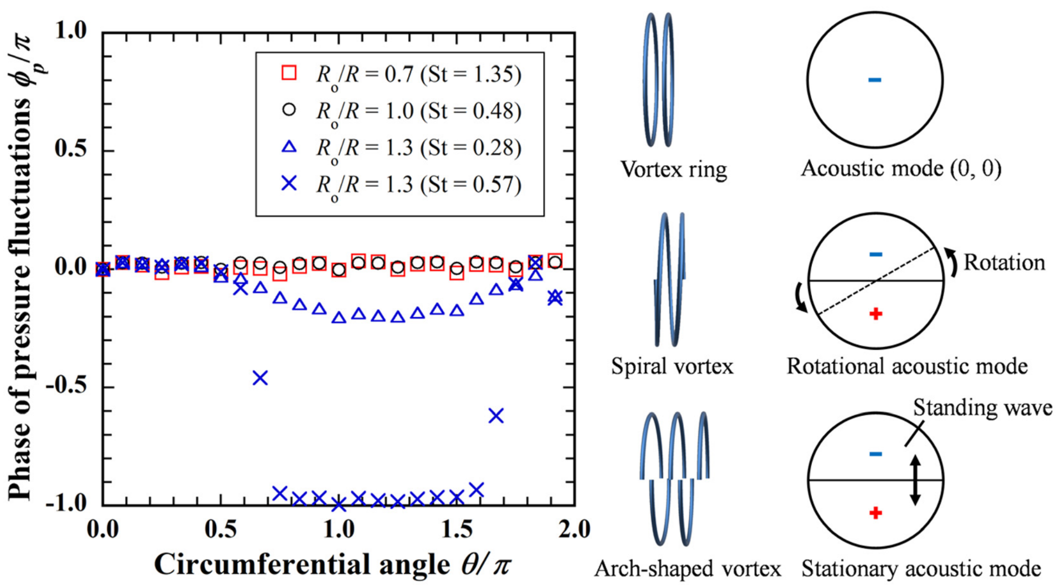

FIG. 17. Predicted phase distribution of pressure fluctuations at Strouhal numbers for intense sounds at the second cavity bottom ($x/L = 0.5$, $r/R_c = 1.0$) at $M = 0.13$ for R_o/R of 0.7, 1.0, and 1.3 with reference to the phase at $\theta = 0$ with images of the relationship between vortical structures and acoustic modes.

shown in Fig. 18(a), the expansion and compression occur around the second orifice in the second and third cavities due to the collision of the vortex ring with the second orifice plate for $R_o/R = 0.7$, while intense pressure fluctuations do not appear in the first cavity. As shown in the right figure of Fig. 18(a), circumferentially in-phase acoustic particle velocity occurs due to the in-phase sound pressure fluctuations on the cross section of downstream surface of the first orifice plate ($x/L = 0.34$). As a result, the shedding of vortex rings is excited due to the acoustic feedback. The sound is intensely propagated into the downstream pipe for $R_o/R = 0.7$ compared with the case of $R_o/R = 1.0$, shown in Fig. 9. This is possibly because the orifice edge, which becomes the position of the main acoustic source due to the collision of the vortices, is protruded in the radially inside direction for the downstream pipe for the small orifice radius of $R_o/R = 0.7$, and the sound is directly propagated into the downstream pipe without the interference of sound with the downstream edge of the expanding pipe. For the larger orifice radius of $R_o/R = 1.3$, the arch-shaped vortices with low-pressure regions collide only with the downstream edge

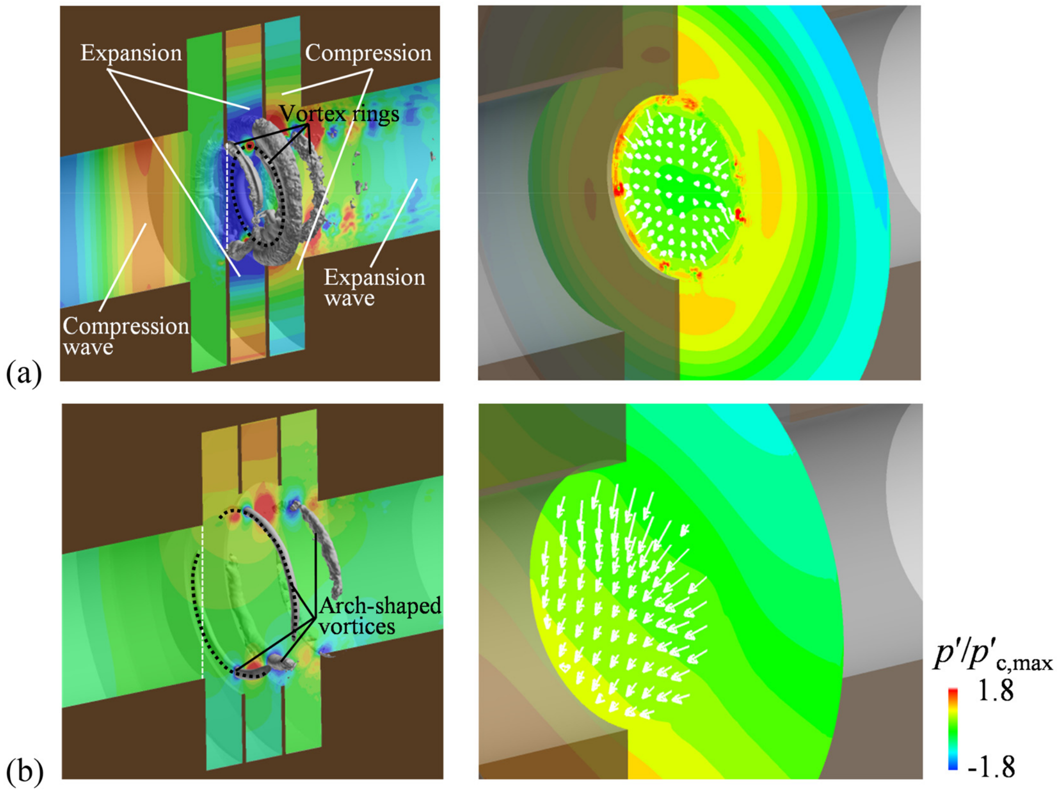

FIG. 18. Phase-averaged flow and pressure fields, where left figures show the contours of fluctuation pressure p' on the x–r plane and iso-surfaces of fluctuation pressure $p'/0.5\rho U_0^2 = -0.3$ (gray) at time for the highest pressure on the second cavity bottom ($t = 0$), $p'_{\mathrm{c,max}}$ ($x/L = 0.5$, $r/R_{\mathrm{c}} = 1.0$, $\theta = \pi/2$), and right figures show the contours of fluctuation pressure and fluctuation velocity vectors at $t/T = 0.25$ on the cross section indicated by white broken lines in the left figures. (a) $R_{\mathrm{o}}/R = 0.7$ (St $= 1.35$, $p'_{\mathrm{c,max}} = 150$ Pa), where right figure shows the contours at the downstream surface of the first orifice plate ($x/L = 0.34$). (b) $R_{\mathrm{o}}/R = 1.3$ (St $= 0.28$, $p'_{\mathrm{c,max}} = 193$ Pa), where right figure shows the contours at the expanding pipe inlet ($x = 0$).

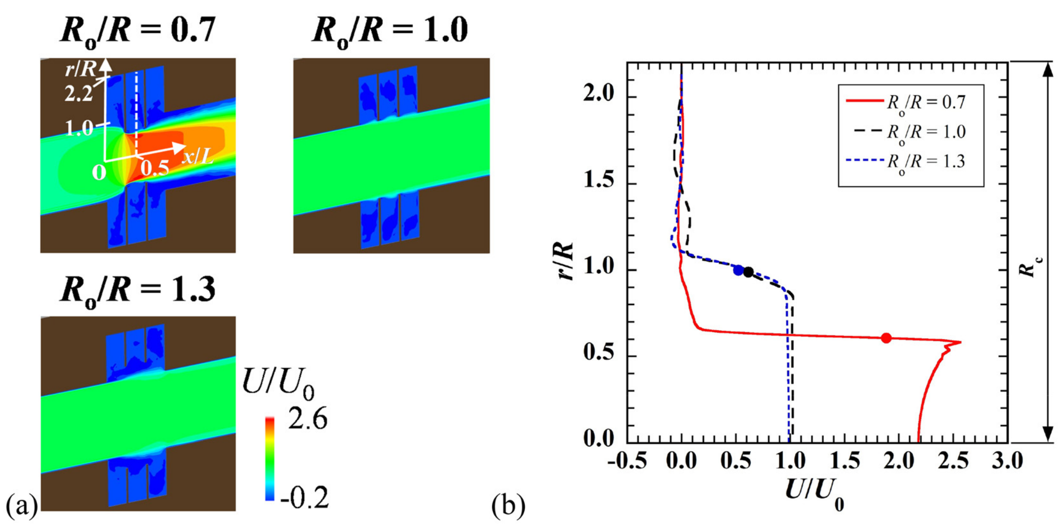

FIG. 19. Mean flow field at $M = 0.13$. (a) Contours of the mean streamwise velocity, U, on the x–r plane. (b) Radial profiles of the mean streamwise velocity along the centerline of the second cavity ($x/L = 0.5$), where circles indicate the positions for the most intense power of velocity fluctuations at the fundamental Strouhal number.

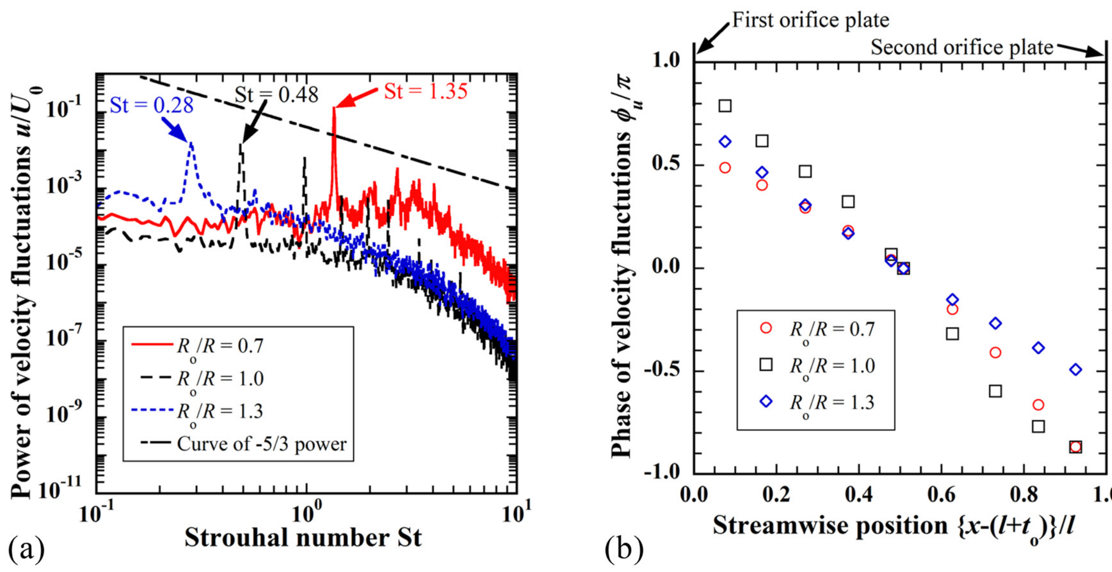

FIG. 20. Predicted streamwise velocity fluctuations u in and around the second cavity at $M = 0.13$. (a) Power spectra at the radial position for the most intense power at the fundamental Strouhal number of $r/R = 0.67$, 0.99, and 1.00 for $R_o/R = 0.7$, 1.0, and 1.3, respectively, as indicated by circles in Fig. 19(b) ($x/L = 0.5$). (b) Streamwise phase distributions at the fundamental Strouhal number of St = 1.35, 0.48, and 0.28 for $R_o/R = 0.7$, 1.0, and 1.3, respectively.

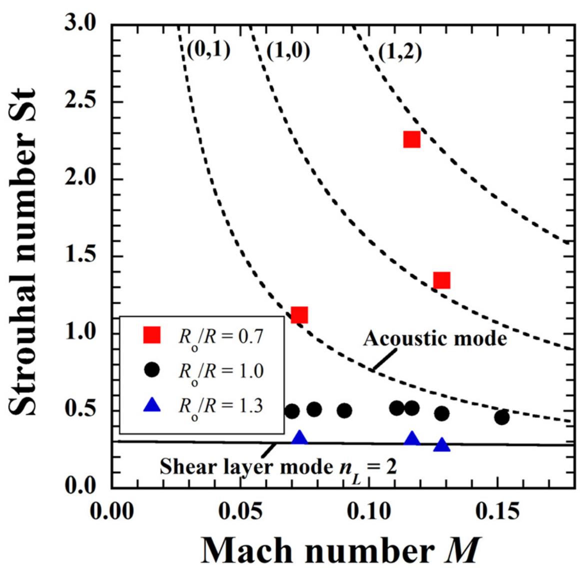

FIG. 21. Predicted variations of the fundamental Strouhal number, which corresponds to that for the most intense sound on downstream pipe wall ($x/L = 1.7$, $r/R = 1.0$), with freestream Mach number, where the curves for acoustic and Rossiter modes based on the length of expanding pipe L are also shown.

of the expanding pipe leading to the acoustic source, while the interactions of the vortices with the orifice plates become weak compared with the other smaller orifice radii ($R_o/R = 0.7$ and 1.0). As shown in the right figure of Fig. 18(b), one-dimensional acoustic particle velocity occurs in the cross section due to the acoustic mode (0, 1) on the cross section of expanding pipe inlet ($x = 0$). The arch-shaped vortices are shed due to the acoustic feedback by the stationary acoustic mode.

2. Effects of orifice radius on flow fields

In this section, the effects of orifice radius R_o on the flow fields in self-sustained oscillations ($M = 0.13$) are discussed. Figure 19(a) shows the contours of the time-averaged (mean) streamwise velocity, U, on the x–r plane. It is presented that the accelerated flow is interfered with the first orifice plate for the smaller radius of $R_o/R = 0.7$. Figure 19(b) shows the radial profiles of the mean streamwise velocity along the centerlines of the second cavity ($x/L = 0.5$). The mean velocity is accelerated to $2.6U_0$ ($M = 0.33$) at $r/R = 0.6$ for $R_o/R = 0.7$, which leads to the higher convection velocity of vortex U_c and the occurrence of the acoustic radiation at a higher Strouhal number, as shown in Fig. 16. The instantaneous local maximum Mach number around the first orifice plate was found to be $M = 0.45$ due to the velocity fluctuations. For the larger radius of $R_o/R = 1.3$, the orifice plates are embedded in the regions with the decreased velocity, leading to the weak interactions of the free shear layer with the orifice plates, where the acoustic feedback loop is formed between the upstream and downstream edges of the expanding pipe.

Figure 20(a) shows the power spectra of the velocity fluctuations in and around the second cavity ($x/L = 0.5$) at the radial position for the maximum power at the fundamental Strouhal numbers of St = 1.35, 0.48, and 0.28 for $R_o/R = 0.7$, 1.0, and 1.3, respectively. As shown in Fig. 20(a), a peaked power appears at each fundamental Strouhal number for all orifice radii, which indicates the occurrence of periodic vortex shedding. In particular, an intense peak appears for $R_o/R = 0.7$ compared with the other orifice radii. This is possibly related to the steep velocity gradient formed in the free shear layer owing to the flow acceleration, as shown in Fig. 19(b).

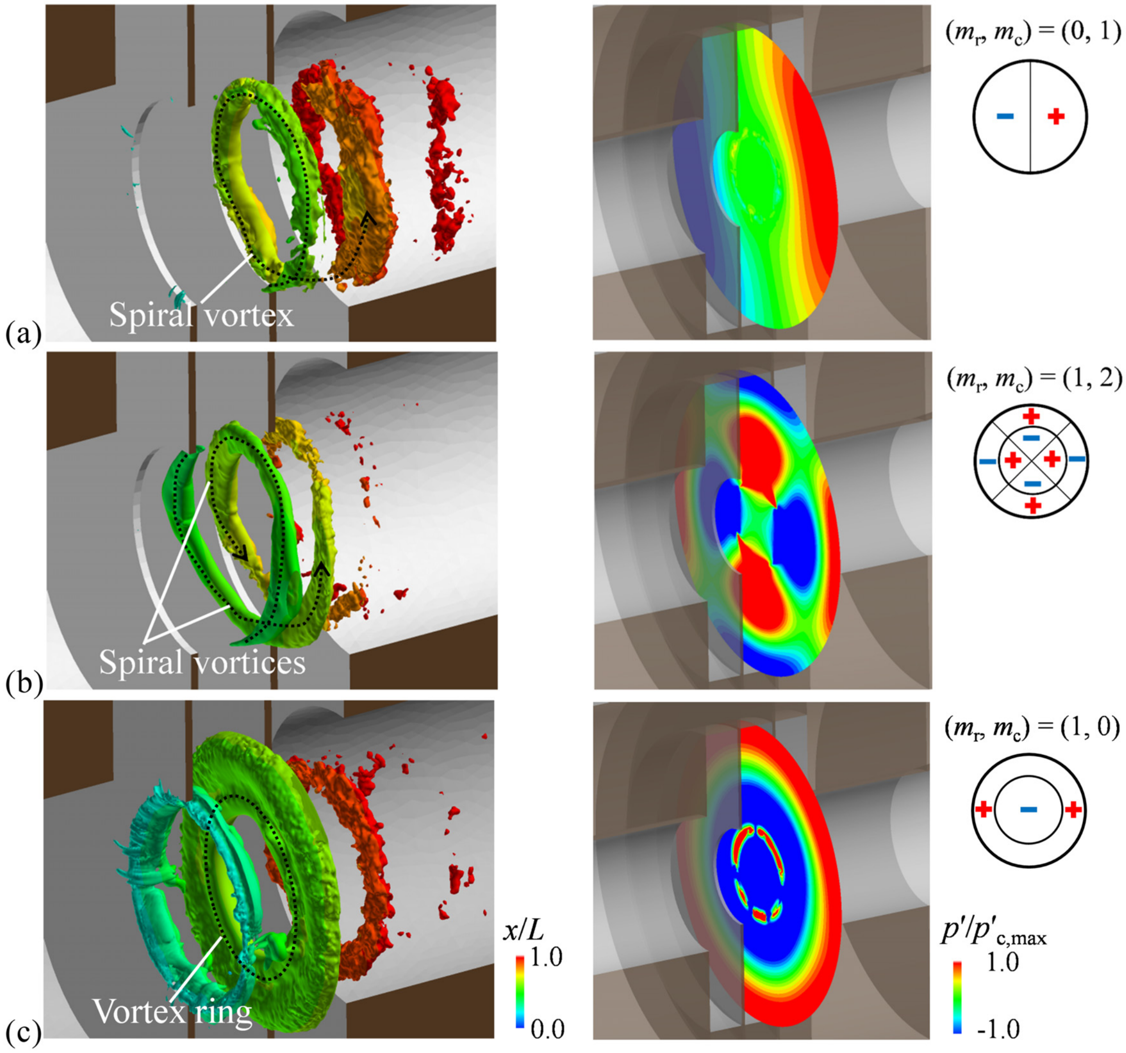

FIG. 22. Phase-averaged flow and pressure fields for the fundamental Strouhal number for $R_o/R = 0.7$, where left figures show the iso-surfaces of low fluctuation pressure, $p'/0.5\rho U_0^2 = -0.3$ colored by x/L, and right figures show the contours of fluctuation pressure, $p'/p'_{c,max}$ ($x/L = 0.5$, $r/R_c = 1.0$, $\theta = 0$), on the cross section of the second cavity ($x/L = 0.5$) along with images of acoustic modes. (a) $M = 0.07$ and St $= 1.12$ ($p'_{c,max} = 200$ Pa). (b) $M = 0.12$ and St $= 2.26$ ($p'_{c,max} = 180$ Pa). (c) $M = 0.13$ and St $= 1.35$ ($p'_{c,max} = 150$ Pa).

Figure 20(b) shows the streamwise phase distributions of the velocity fluctuations, u, at the fundamental Strouhal number in the shear layer in the expanding pipe. Based on the slope of the phase distributions, the ratio of the convection velocity of vortices U_c to freestream velocity U_0 are estimated to be 1.6, 0.6, and 0.5, for $R_o/R = 0.7$, 1.0, and 1.3, respectively. The convection velocity of vortices becomes high particularly for the small orifice radius of $R_o/R = 0.7$. This is consistent with the occurrence of the accelerated flow for $R_o/R = 0.7$, as shown in Fig. 19.

3. Shear layer and acoustic modes with different orifice radii

Figure 21 shows the variations of the predicted fundamental Strouhal number (Strouhal number for the most intense sound in the downstream pipe) with the freestream Mach number. In the case of $R_o/R = 1.0$, the fundamental Strouhal number is constant at almost St $= 0.5$ for all Mach numbers. This is because of the occurrence of the Rossiter mode of $n = 1$ in each cavity, as discussed in Sec. III B.

For the smaller orifice radius of $R_o/R = 0.7$, the fundamental Strouhal number jumps with the variation of the freestream Mach number, as shown in Fig. 21. Figure 22 shows vortices (left) and contours of fluctuation pressure (right) for the phase-averaged flow fields at the fundamental Strouhal number for $R_o/R = 0.7$. It is shown that the vortical structures and acoustic mode depend on the freestream Mach number. Figure 22(a) shows that one spiral vortex is shed in the second cavity, which collides with the second orifice plates exciting the acoustic mode (0, 1) at $M = 0.07$. Figures 22(b) and 22(c) show that two spiral vortices and one vortex ring are shed in the shear layer of the second cavity at the higher Mach numbers of $M = 0.12$ and 0.13, leading to the excitation of acoustic modes (1, 2) and (1, 0), respectively. Figure 21 also shows the curves of the Strouhal numbers for the acoustic modes estimated by Eq. (5) ($\varepsilon = 1.1$), and the fundamental Strouhal number is confirmed to approximately lie on the curves of these acoustic modes. The acoustic resonance with a high acoustic mode (1, 2) occurs because the oscillations with the shear layer mode [see Eq. (4)] occur at a high Strouhal number for $R_o/R = 0.7$ owing to the high convection velocity in the accelerated flow, as shown in Fig. 20.

As shown in Fig. 21, for the large orifice radius of $R_o/R = 1.3$, the fundamental Strouhal number is constant at almost 0.3 for all Mach numbers. Figure 21 also shows the curve for the Strouhal number for the second Rossiter mode taking the streamwise total expanding pipe length L as the cavity length of $n_L = 2$, which is estimated by Eq. (6). In Eq. (6), the values of κ and γ are set to 0.5 and 0.1 referring to the convection velocity for $R_o/R = 1.3$ discussed in Sec. III C 2

$$\mathrm{St} = \frac{l}{L}\frac{fL}{U_0} = \frac{l}{L}\frac{n_L - \gamma}{1/\kappa + M}. \tag{6}$$

As shown in Fig. 21, the fundamental Strouhal number for $R_o/R = 1.3$ approximately lies on the curve for $n_L = 2$ at all Mach numbers. This indicates the formation of the feedback loop between the upstream and downstream edges of the expanding pipe, where the acoustic feedback and radiation occur at the upstream and downstream edges, respectively.[4,5] This is consistent with the vortical behaviors for $R_o/R = 1.3$, as shown in Fig. 18(b).

As described in this section, vortical structures and interactions between the vortices and orifice plates in the shear layer mode are affected by the orifice radius. As a result, the coupling mechanism of shear layer and acoustic modes is also varied.

IV. CONCLUSIONS

To clarify the generation mechanism and conditions for the intense acoustic radiation from a flow around an expanding pipe with two orifice plates, the flow and acoustic fields were predicted with different inflow Mach numbers and three ratios of the orifice radius to the upstream and downstream pipe radius of $R_o/R = 0.7$, 1.0, and 1.3 based on compressible flow simulations.

The present computational results show that the tonal sound radiation occurs owing to the shear layer mode with vortex shedding in the free shear layer in the expanding pipe with the orifice plates. This shear layer mode occurs in each cavity separated by the orifice plates for $R_o/R = 0.7$ and 1.0, where the collision of the vortices with the orifice plates and the downstream edge of the expanding pipe leads to the acoustic radiation. Meanwhile, the interactions between vortices and orifice plates become weaker and the acoustic radiation occurs mainly around the downstream edges of the expanding pipe for the larger orifice radius of $R_o/R = 1.3$.

The acoustic resonance can also occur with different acoustic modes depending on the orifice radius and freestream Mach number, which causes a steep change of the fundamental frequency with the freestream Mach number. The coupling between the shear layer and acoustic modes leads to the occurrence of fluid-resonant oscillations with the intense acoustic radiation. The formation of a spiral vortex and vortex ring for the shear layer mode causes the circumferentially varied-phase and in-phase sound pressure fluctuations in the expanding pipe, respectively. The in-phase pressure fluctuations are more intensely propagated outside the expanding pipe into the downstream pipe compared with those with varied-phase distributions. In addition, the convection velocity of the vortices becomes higher in the accelerated flow for the small orifice radius of $R_o/R = 0.7$, leading to the occurrence of acoustic modes with higher frequencies.

To the best of the authors' knowledge, this is the first study to clarify the flow and acoustic fields around the expanding pipe with orifice plates. These results do not merely present useful knowledge for the design of the silencer consisting of the expanding pipe with orifice plates, but also interesting phenomena of the fluid-resonant oscillations with variation of vortical structures and acoustic mode in circular cavity flows.

ACKNOWLEDGMENTS

This work was partly supported by JSPS KAKENHI Grant No. 21K03874. Computational resources through the HPCI System Research Project (Project ID: hp230012) were also used.

AUTHOR DECLARATIONS

Conflict of Interest

The authors have no conflicts to disclose.

Author Contributions

Akitomo Fukuma: Data curation (lead); Investigation (lead); Methodology (equal); Validation (equal); Visualization (equal); Writing – original draft (lead). **Manato Kawai:** Data curation (supporting); Validation (equal). **Nini Furukawa:** Data curation (supporting); Validation (supporting). **Kenji Kawasaki:** Investigation (equal); Writing – review & editing (supporting). **Ichiro Yamagiwa:** Investigation (supporting); Writing – review & editing (supporting). **Masahito Nishikawara:** Investigation (supporting); Writing – review & editing (supporting). **Hiroshi Yokoyama:** Conceptualization (lead); Data curation (equal); Funding acquisition (lead); Investigation (equal); Methodology (equal); Software (lead); Supervision (lead); Writing – original draft (equal); Writing – review & editing (lead).

DATA AVAILABILITY

The data that support the findings of this study are available from the corresponding author upon reasonable request.

REFERENCES

[1] M. Cervenka, M. Bednarik, and J. P. Groby, "Optimized reactive silencers composed of closely-spaced elongated side-branch resonators," J. Acoust. Soc. **145**, 2210–2220 (2019).
[2] H. Shahzad, S. Hickel, and D. Modesti, "Turbulence and added drag over acoustic liners," J. Fluid Mech. **965**, A10 (2023).
[3] J. E. Rossiter, "Wind-Tunnel experiments on the flow over rectangular cavities at subsonic and transonic speeds," Aeronautical Research Council Reports and Memoranda No. 3438, 1964.
[4] C. W. Rowley, T. Colonius, and A. J. Basu, "On self-sustained oscillations in two-dimensional compressible flow over rectangular cavities," J. Fluid Mech. **455**, 315 (2002).
[5] H. Yokoyama and C. Kato, "Fluid-acoustic interactions in self-sustained oscillations in turbulent cavity flows. I. Fluid-dynamic oscillations," Phys. Fluids **21**, 105103 (2009).

[6]S. Ziada, H. Ng, and C. E. Blake, "Flow excited resonance of a confined shallow cavity in low Mach number flow and its control," J. Fluids Struct. **18**, 79–92 (2003).

[7]P. Wang and Y. Liu, "Intensified flow dynamics by second-order acoustic standing-wave mode: Vortex-excited acoustic resonances in channel branches," Phys. Fluids **31**, 035105 (2019).

[8]Y. W. Ho and J. W. Kim, "A wall-resolved large-eddy simulation of deep cavity flow in acoustic resonance," J. Fluid Mech. **917**, A17 (2021).

[9]D. Rockwell and E. Naudascher, "Review—Self-sustaining oscillations of flow past cavities," ASME Trans. J. Fluids Eng. **100**, 152–165 (1978).

[10]K. Aly and S. Ziada, "Flow-excited resonance of trapped modes of ducted shallow cavities," J. Fluids Struct. **26**, 92–120 (2010).

[11]K. Aly and S. Ziada, "Azimuthal behaviour of flow-excited diametral modes of internal shallow cavities," J. Sound Vib. **330**, 3666–3683 (2011).

[12]P. Wang and Y. Liu, "Influence of diametral acoustic mode on cavity flow dynamics: Zonal large eddy simulation and proper orthogonal decomposition," Phys. Fluids **32**, 075103 (2020).

[13]P. Wang and Y. Liu, "Spinning behaviour of flow-acoustic resonant fields inside a cavity: Vortex-shedding modes and diametral acoustic modes," Phys. Fluids **32**, 085109 (2020).

[14]M. Abdelmwgoud, M. Shaaban, and A. Mohany, "Flow dynamics and azimuthal behavior of the self-excited acoustic modes in axisymmetric shallow cavities," Phys. Fluids **32**, 115109 (2020).

[15]K. Matsuura and M. Nakano, "Direct computation of a hole-tone feedback system at very low Mach numbers," J. Fluid Sci. Technol. **6**, 548–561 (2011).

[16]K. Matsuura and M. Nakano, "A throttling mechanism sustaining a hole tone feedback system at very low Mach numbers," J. Fluid Mech. **710**, 569–605 (2012).

[17]M. Sano and T. Oyaizu, "Transition process of frequencies of pure tone caused by vortex shedding in a pipeline containing a double orifice," J. Environ. Eng. **3**, 228–239 (2008).

[18]A. Fukuma, H. Yokoyama, M. Kawai, K. Kawasaki, I. Yamagiwa, M. Nishikawara, and H. Yanada, "Direct aeroacoustic simulation of a flow through an expanding pipe with orifice plates," in Proceedings of Inter-Noise, 2023.

[19]H. Yokoyama, K. Otsuka, K. Otake, M. Nishikawara, and H. Yanada, "Control of cavity flow with acoustic radiation by an intermittently driven plasma actuator," Phys. Fluids **32**, 106104 (2020).

[20]Q. Liu and O. V. Vasilyev, "A Brinkman penalization method for compressible flows in complex geometries," J. Comput. Phys. **227**, 946–966 (2007).

[21]H. Yokoyama, A. Miki, H. Onitsuka, and A. Iida, "Direct numerical simulation of fluid–acoustic interactions in a recorder with tone holes," J. Acoust. Soc. **138**, 858–873 (2015).

[22]H. Yokoyama, K. Minowa, K. Orito, M. Nishikawara, and H. Yanada, "Compressible simulation of flow and sound around a small axial-flow fan with flow through casing slits," J. Fluids Eng. **142**(10), 101215 (2020).

[23]S. K. Lele, "Compact finite difference schemes with spectral-like resolution," J. Comput. Phys. **103**, 16–42 (1992).

[24]K. Matsuura and C. Kato, "Large-eddy simulation of compressible transitional flows in a low-pressure turbine cascade," AIAA J. **45**, 442–457 (2007).

[25]D. V. Gaitonde and M. R. Visbal, "Pade-type higher-order boundary filters for the Navier-Stokes equations," AIAA J. **38**, 2103–2112 (2000).

[26]J. W. Kim and D. J. Lee, "Generalized characteristic boundary conditions for computational aeroacoustics," AIAA J. **38**, 2040–2049 (2000).

[27]K. Terao, H. Yokoyama, Y. Ogoe, and A. Iida, "Proposition of a new formula for frequency prediction based on generation mechanism of aerodynamic sound in cavity flows," Trans. Jpn. Soc. Mech. Eng. B **77**, 1522–1532 (2011) (in Japanese).

[28]H. Yokoyama, Y. Omori, M. Kume, M. Nishikawara, and H. Yanada, "Simulation of thermoacoustic heat pump effects driven by acoustic radiation in a cavity flow," Int. J. Heat Mass Transfer **185**, 122424 (2022).

[29]M. J. Zucrow and J. D. Hoffman, *Gas Dynamics*, Multidimensional Flow Vol. 2 (John Wiley and Sons, Inc., 1977).